Computers and Fluids 263 (2023) 105945

Contents lists available at ScienceDirect

Computers and Fluids

journal homepage: www.elsevier.com/locate/compfluid

High-fidelity simulations of the aeroacoustic environment of the VEGA launch vehicle at lift-off

Giacomo Della Posta [a,*], Emanuele Martelli [c], Fulvio Stella [a], Daniele Barbagallo [b], Agostino Neri [b], Francesco Salvadore [d], Matteo Bernardini [a]

[a] Sapienza University of Rome, via Eudossiana 18, Rome (RM), 00184, Italy
[b] European Space Agency, via Galileo Galilei 1, Frascati (RM), 00044, Italy
[c] Politecnico di Torino, Corso Duca degli Abruzzi 24, Torino (TO), 10129, Italy
[d] HPC Department, CINECA, via dei Tizii 6,/B, Rome (RM), 00185, Italy

ARTICLE INFO

MSC:
76Q05

Keywords:
Aeroacoustics
Space launcher lift-off
Ignition/duct overpressure
Large eddy simulations
Immersed boundary method
GPU/CPU accelerated solver

ABSTRACT

The lift-off of space launch vehicles generates strong acoustic waves that interact in a complex and potentially dangerous way with the launch facility and the launcher itself. Engineering tools developed in the past to predict the strong acoustic radiation and the peak acoustic loads during the first seconds of the launch have a limited validity and are not able to provide reliable predictions. For this reason, in order to better identify the noise generation sources and to assess the effects of acoustic mitigation measures, it is fundamental to develop and validate more advanced computational models able to capture the transient flow induced by the ignition of the motors. In this work, we present high-fidelity 3D Large Eddy Simulations of the acoustic field produced by the lift-off of a realistic space launcher. A state-of-the-art, high-order, GPU accelerated, compressible solver is used to simulate the highly unsteady interaction of the exhaust plume from the launcher's nozzle with a realistic launch pad, whose geometry has been modelled by Immersed Boundary Method. The results obtained demonstrate the capability of our solver to provide accurate predictions compared to flight measurements of real configurations, despite the challenging scenario in terms of operating conditions and geometry. Moreover, wavelet analysis proves to be an appropriate tool to pinpoint and characterise the overpressure mechanisms that take place in the transient evolution of the flow.

1. Introduction

Despite its short duration, the lift-off represents a critical phase for space launchers, with violent aeroacoustic phenomena that can potentially harm the integrity of the payload dramatically [1,2]. More precisely, during the very first seconds of the launch, the impulsive ignition of the solid rocket motors (SRMs) induces strong pressure waves that can travel along the launcher and in the fluid field, inducing significant pressure loads on the fairing and on the delicate and expensive payload inside it. Researchers agree to attribute the generated aeroacoustics phenomena mainly to two mechanisms: the ignition overpressure (IOP) and the duct overpressure (DOP) [2]. According to the IOP mechanism, shown in Fig. 1(a), the supersonic flow ejected from the nozzle outlet impinges on the wall of the flame deflector and generates reflected pressure waves that travel upwards and reach the fairing, if the launch pad is open. On the other hand, according to the DOP mechanism, shown in Fig. 1(b), the deflected plume exits from the exhaust ducts and interacts also with the lip of the ducts themselves, generating pressure waves that travel towards the launcher as well.

Many studies, both experimental and numerical, have tried to describe and predict these phenomena, see Jiang et al. [3] for a review. Field measurements [1,4] certainly represent the most representative way to obtain information about the real conditions in the real environment, but they are demanding, expensive, and hardly available. Several reduced-scale experiments [5–7] have been conducted under controlled conditions, but scale similarity is difficult to maintain. For this reason, numerical simulations represent a promising alternative for the estimation and characterisation of the IOP/DOP mechanisms [8]. High-fidelity simulations of acoustic fields represent a challenging and computationally onerous task for computational fluid dynamics (CFD) since the flows that generate noise are usually nonlinear, unsteady and turbulent [9]. Furthermore, the launch environment introduces additional and specific issues with respect to typical aeroacoustics

* Corresponding author.
E-mail addresses: giacomo.dellaposta@uniroma1.it (G. Della Posta), emanuele.martelli@polito.it (E. Martelli), fulvio.stella@uniroma1.it (F. Stella), daniele.barbagallo@ext.esa.int (D. Barbagallo), agostino.neri@esa.int (A. Neri), f.salvadore@cineca.it (F. Salvadore), matteo.bernardini@uniroma1.it (M. Bernardini).

https://doi.org/10.1016/j.compfluid.2023.105945
Received 14 November 2022; Received in revised form 28 April 2023; Accepted 30 May 2023
Available online 5 June 2023

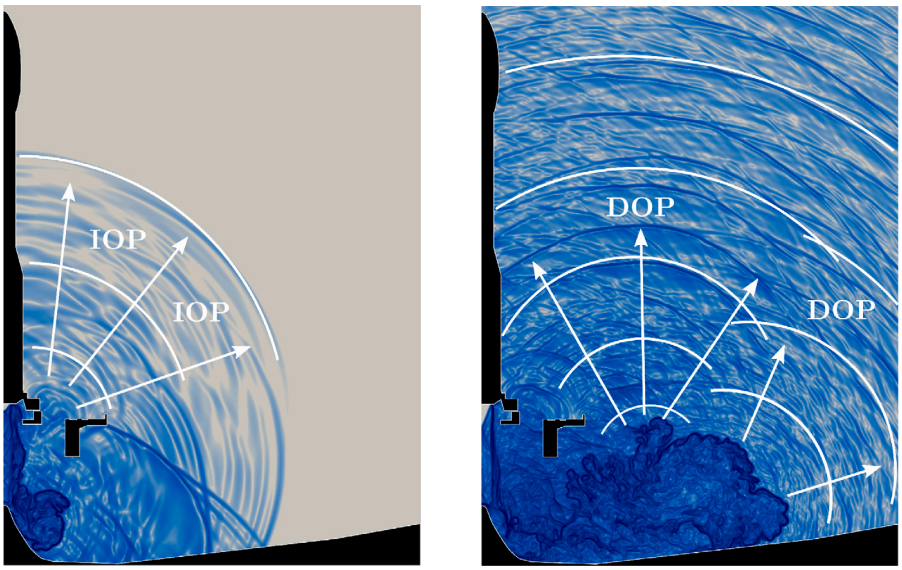

(a) IOP (b) DOP

Fig. 1. Ignition/duct overpressure induced during the lift-off of a space launcher.

problems, associated with the wide range of spatial and temporal scales present during the lift-off of a space vehicle. Several works considered simplified, fundamental configurations with imposed conditions for free jets [10–12] or impinging jets, both on normal [13,14] and inclined plates [15–17]. However, although the physical analysis is certainly precious, the conclusions can suffer from oversimplification with respect to the real flow case. For this reason, some research groups tried to simulate the actual configuration of the full launch pad [18,19], in an attempt to provide full field data accessibility under real conditions. However, the computational burden and the complexity of the methodology necessary to deal with such a complicated geometry and challenging conditions hinder a complete and accurate simulation of the case: it is no wonder that the effective use of a single, unsteady, high-fidelity CFD simulation of this specific complex aerospace system is taken as a case in point to assess the development of CFD tools by the CFD Vision 2030 programmatic study [20]. Various approaches have been adopted to tackle the problem, which range from inviscid simulations [21] or steady and unsteady Reynolds averaged Navier–Stokes simulation (RANS) [22,23] to hybrid RANS/large eddy simulation (LES) methods [19], or even acoustic boundary element methodologies [24], in an attempt to identify the most relevant noise sources of the field.

In view of the literature survey, and given the need of improved high-fidelity CFD simulations for this though problem, this work attempts to replicate numerically the aeroacoustics of the earliest instants of the lift-off, for real conditions and a real geometrical configuration, by means of a flow solver that exploits the computational acceleration provided by graphics processing units (GPUs). For our case, we consider the VEGA space launcher developed by the European Space Agency (ESA) [25] and an open launch pad geometry inspired to the Europe's Spaceport in Kourou, French Guiana (see Fig. 2 for the nomenclature of the various parts of the launch pad). In order to characterise the unsteady behaviour of the flow, after having described qualitatively its evolution, we characterise the pressure in time and frequency in correspondence of two specific probes on the fairing by comparing the results with the flight data provided by ESA, recorded during 2012's VEGA launch VV01 [26]. In addition to the analysis in the Fourier domain, we also present an analysis in the time/time-scale domain by means of the wavelet transform. Several examples in the literature demonstrated the added value of wavelet analysis [27–32], but none of the previous works that attempted to simulate the entire launch pad have carried out such an analysis to study the IOP/DOP mechanism.

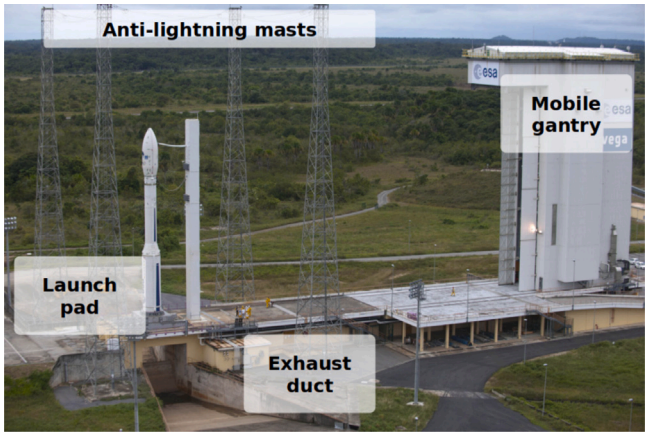

Fig. 2. The Vega 1 rocket on the launch pad of the Europe's Spaceport in Kourou, French Guiana and nomenclature of the various parts of the launch pad. [33].

The paper is organised as follows: Section 2 presents the numerical methodology adopted for the simulations; Section 3 describes the case considered and the computational setup devised for the computations; Section 4 presents the analysis of the results, reporting a detailed time–frequency investigation of both numerical pressure signals and flight data. Section 5 reports some final comments.

2. Methodology

The generation of acoustic waves is intrinsically related to unsteady processes, and sound is not produced by a steady flow. As a consequence, all turbulence modelling approaches based on RANS equations, which filter small spatial scales and high-frequency fluctuations, are not suitable for aeroacoustic simulations. Direct numerical simulations (DNSs) resolving all the relevant scales of motion, would be the ideal candidate to fully capture the sound generation, but their feasibility for practical applications at high Reynolds number, is still faraway due to the huge number of grid nodes required. In this context, the LES approach, which allows to directly compute on the grid the energetically relevant scales of the flow, represents an excellent compromise between accuracy and computational cost.

Accurately predicting sound generation is essential but represents only one of the ingredients of an aeroacoustics computation. Since acoustic waves propagate with very low attenuation over long distances, numerical methods suitable for aeroacoustics simulation must comply with strict requirements that guarantee very low levels of numerical dispersion and dissipation.

The exhaust plume of a rocket motor is highly overexpanded and characterised by a complex pattern with multiple shock waves interacting with the small scale vortical structures of the turbulent shear layers. This scenario is very challenging from the computational point of view and involves the use of extremely robust discretisation algorithms, a requirement potentially in conflict with those previously highlighted for the sound propagation.

Further complication is caused by the launch environment, typically characterised by a very complex geometry, which is an additional and important challenge for CFD given the considerable difficulties to obtain good accuracy in combination with unstructured or overlapping body fitted grids.

The method we have devised for an accurate and efficient solution of the issues listed above relies on the capabilities of the flow solver STREAmS [34–36], developed at Sapienza University of Rome and freely available in its baseline version on github.[1]

The code allows to perform DNSs or LESs of the Navier–Stokes equations for high-speed turbulent flows with calorically or thermally perfect gas on Cartesian grids. The governing equations are thus:

$$\frac{\partial \rho}{\partial t} + \frac{\partial \rho u_i}{\partial x_i} = 0\,, \tag{1a}$$

$$\frac{\partial \rho u_i}{\partial t} + \frac{\partial \rho u_i u_j}{\partial x_j} = -\frac{\partial p}{x_i} + \frac{\partial \sigma_{ij}}{\partial x_j}\,, \tag{1b}$$

$$\frac{\partial \rho E}{\partial t} + \frac{\partial \rho u_j H}{\partial x_j} = -\frac{\partial q_j}{x_j} + \frac{\partial \sigma_{ij} u_i}{\partial x_j}\,, \tag{1c}$$

where u_i is the velocity component along the ith coordinate direction, ρ is the density, $E = e(T) + u_i u_i/2$ is the total energy per unit mass with $e(T)$ being the internal energy, and $H = E + p/\rho = h + u_i u_i/2$ is the total enthalpy. Viscous stress tensor σ_{ij} is expressed according to Boussinesq approximation, where dynamic viscosity μ is evaluated through Sutherland's law. Heat flux vector is expressed according to Fourier law, where thermal conductivity k is equal to $C_p\mu/Pr$, with constant Prandtl number $Pr = 0.72$ and with temperature-dependent specific heat C_p. All the simulations reported in this work are performed by relying on the implicit large eddy simulation (ILES) approach [37]. In contrast to classical LES, that employs an explicit subgrid-scale (SGS) model, ILES is based on the embedded regularisation mechanism arising from the discretisation of the convective terms. Several studies [17,38,39] have confirmed that for turbulent flows away from physical boundaries, the ILES approach is able to exploit efficiently the grid resolution to describe the essential behaviour of turbulent flows and the transition of the shear layers.

Concerning the numerical methods, STREAmS implements high-order finite difference schemes. In the general case, the convective terms in the Navier–Stokes equations are discretised using a hybrid energy preserving/shock-capturing discretisation algorithm [40]. Shock-capturing is achieved using the Lax–Friedrichs flux vector splitting, whereby the components of the positive and negative characteristic fluxes are reconstructed at the interfaces using a fifth-order, weighted-essentially non-oscillatory (WENO) reconstruction [41]. When running in ILES mode, the energy-preserving scheme is deactivated and WENO reconstructions are applied everywhere to discretise the convective fluxes and provide the amount of numerical dissipation required by ILES. In particular, all the simulations here reported have been performed using the improved fifth-order WENO-Z scheme proposed by Borges et al. [42]. The viscous terms are expanded to Laplacian form to avoid odd-even decoupling phenomena and then approximated with sixth-order formulas. Time advancement is carried out by means of a three-stage, third-order Runge–Kutta scheme.

The current version of the solver, named STREAmS-2.0, is written in Fortran 2008 following an object-oriented style in order to allow the implementation of different equations and support multiple computational backends minimising code duplication. The computational kernels are implemented as pure functions (not using global data) in order to make them suitable for specific optimisations including possible translations into other languages, in particular C. All the simulations reported in this work have been performed using the CUDA Fortran backend capable of taking advantage of NVIDIA GPUs. The CUDA Fortran paradigm allows the user to achieve optimal performance while maintaining good readability of the code that remains entirely in Fortran. A significant number of kernels have been implemented through cuf kernels, therefore automatic, while explicit kernels have been considered more appropriate for more complex parts of code, such as convective kernels that include WENO shock-capturing methodologies. Concerning I/O management, three-dimensional fields are efficiently handled thanks to the implementation of standard MPI/IO routines.

Table 1
Iteration elapsed time for grid 420×250×320 considering three computational backends, namely: Traditional CPU node (2 CPU EPYC 7763), NVIDIA GPU V100, NVIDIA GPU A100.

2 CPU EPYC 7763	GPU V100	GPU A100
2.173	0.948	0.479

Table 1 shows the performance achieved by STREAmS-2.0 considering convective kernels in full-WENO mode, the mode used for the simulations of this work. The reference grid is 420 × 250 × 320. The backends in comparison are a recent CPU node with 2 EPYC 7763 CPUs and two NVIDIA GPUs, V100 and A100. Using one GPU more than halves the elapsed time if compared to a full CPU-only node and, considering that a compute node usually has 4 GPUs, the advantage of using GPU-powered nodes is remarkable.

STREAmS-2.0 is parallelised via MPI to handle different CPUs or GPUs. Fig. 3 shows the scalability of the solver as the number of nodes varies considering the CUDA Fortran backend and the Marconi100 cluster, which is equipped with 4 V100 GPUs per node and which was used to perform the simulations of this work. The trends are shown considering the two communication patterns supported by STREAmS-2.0, namely synchronous and asynchronous, the latter being capable of managing overlap between communications and computation. Strong scaling shows acceptable code efficiency up to 8 nodes (corresponding to one million of grid points per GPU) while weak scaling is close to ideal values up to the maximum number of nodes considered, i.e. 256. The asynchronous pattern allows to significantly improve scalability in roughly all situations considered.

2.1. Immersed boundary methodology

The management of complex geometries relies on the application of a ghost-point-forcing immersed boundary method (IBM) suitable for compressible flows [43,44] already validated in previous works [45,46]. The implementation is characterised by the following steps:

1. a closed 3D surface is provided in standard Stereo-LiThography (STL) format to be immersed in the Cartesian grid.
2. The ray-tracing algorithm of the Computational Geometry Algorithms Library (CGAL) [47] classifies the nodes as solid or fluid nodes, being they inside or outside the geometry respectively.
3. Solid nodes are further split into pure solid and ghost nodes. Ghost nodes are those grid points inside the solid that contribute to the discretisation of the governing equations for some point inside the fluid.

[1] GitHub page: https://github.com/STREAmS-CFD/STREAmS-2

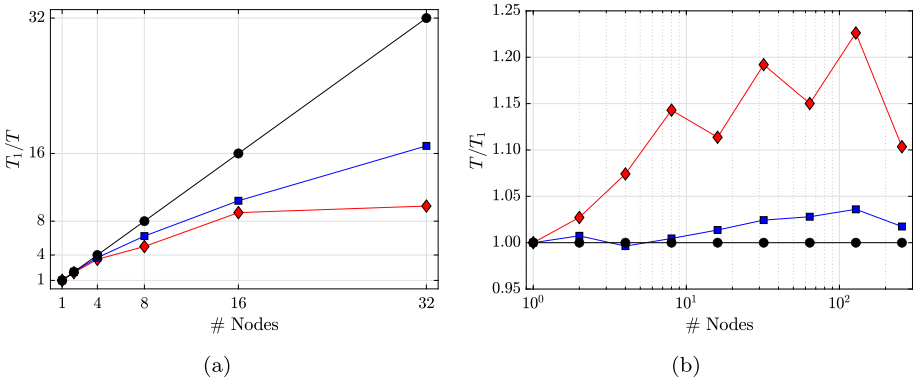

Fig. 3. Strong (a) and weak (b) scalability tests on Marconi100 supercomputing cluster: — ideal scaling, — synchronous communication mode, — asynchronous communication mode.

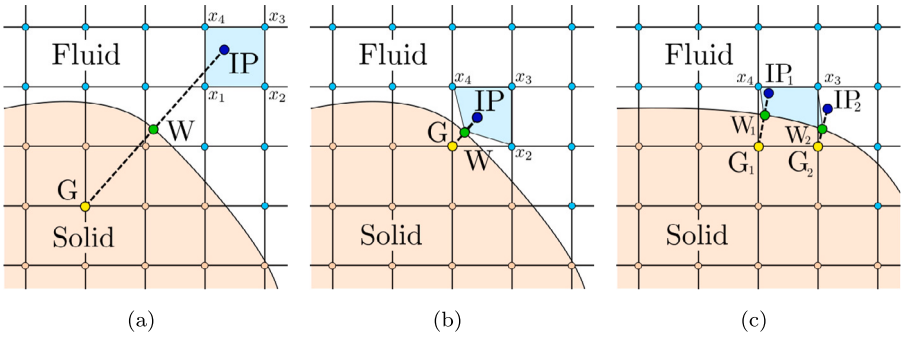

Fig. 4. Sketch of the boundary interpolation for a two-dimensional case. Ghost nodes in yellow, wall nodes in green, image points in blue. Points x_1, x_2, x_3 and x_4 are the vertices used to interpolate the solution at IP, which are substituted by wall points when the surface cuts the interpolation cell (b and c).

4. For each ghost node (G), an image point (IP) along the wall-normal direction is defined (Fig. 4). The values of the generic variable φ at the eight vertices of the cell containing the IP are used to derive the eight coefficients C_i defining trilinear interpolation inside the cell. Thus, if

$$\varphi(x,y,z) = C_1xyz + C_2xy + C_3xz + C_4yz + C_5x + C_6y + C_7z + C_8 \quad (2)$$

and ϕ_i are the values of the variable φ at the eight vertices of the IP cell, the coefficients C_i are obtained by solving the algebraic system

$$[x_iy_iz_i \quad x_iy_i \quad x_iz_i \quad y_iz_i \quad x_i \quad y_i \quad z_i \quad 1]\,C_i = \phi_i \qquad i = 1,\dots,8 \quad (3)$$

To handle possible exceptions making the problem ill-posed, as those illustrated in Fig. 4, wall points are directly included in the interpolation by using their coordinates at the corresponding matrix lines, as described in Piquet et al. [44] and in De Vanna et al. [48].

5. The coefficients are used to interpolate φ at IP, and the conservative variables in the ghost nodes are then assigned to prescribe indirectly the desired boundary conditions at the walls. For example, to impose Dirichlet conditions φ_w at the wall, the ghost node value is equal to

$$\varphi_G = 2\varphi_w - \varphi_{IP} \quad (4)$$

while for Neumann conditions

$$\varphi_G = \varphi_{IP} - |\mathbf{x_{IP}} - \mathbf{x_G}| \left(\frac{\partial\varphi}{\partial\mathbf{n}}\right)_w \quad (5)$$

where $\mathbf{x}$ is the position vector and $\mathbf{n}$ is the normal to the surface pointing towards the fluid.

Table 2
Main features of the adopted numerical setup. Δ_{vol} is the volumetric grid size equal to $(\Delta x\,\Delta y\,\Delta z)^{1/3}$, whereas $\overline{\Delta t}$ is the mean time step used for the simulation.

	$L_x/D \times L_y/D \times L_z/D$	$N_x \times N_y \times N_z$	Δ_{vol}/D	$\overline{\Delta t}\,c_\infty/D$
Mesh A	$23.1 \times 13.1 \times 50.4$	$968 \times 560 \times 2048$	0.024	$9.58 \cdot 10^{-4}$
Mesh B	$23.1 \times 13.1 \times 50.4$	$1888 \times 1072 \times 4096$	0.012	$5.96 \cdot 10^{-4}$

This methodology is used to apply the boundary conditions at the solid walls (zero velocity and null pressure and temperature gradients) and also to impose the supersonic inflow on the nozzle exit patch (see Section 3).

According to Chaudhuri et al. [49], the direct-forcing method, using a fifth-order WENO scheme, is found to converge towards a second-order of accuracy near the boundaries.

3. Case description and numerical setup

When observing the entire launch procedure of VEGA, it is possible to notice that the transient phase of the nozzle flow relevant for the IOP/DOP mechanisms happens in the very first second of the launch, when the motion of the rocket with respect to the launch pad can be neglected. For this reason, we assumed to simulate the realistic configuration with a fixed, non-moving geometry, as shown in Fig. 5. Each simulation considered approximately 1.3 physical seconds.

It should be noted that, for the particular case under study, the gas constant of the exhaust jet is incidentally almost identical to the one of the surrounding air, and the corresponding speeds of sound are very similar at ambient temperature (less than 2% of difference). For this reason and given the large separation in temperature between the hot jet mixture and the cold air outside, it is reasonable for our specific case to model the fluid as a single thermally perfect gas with a specific heat capacity given by a blending of the properties of the air for cold

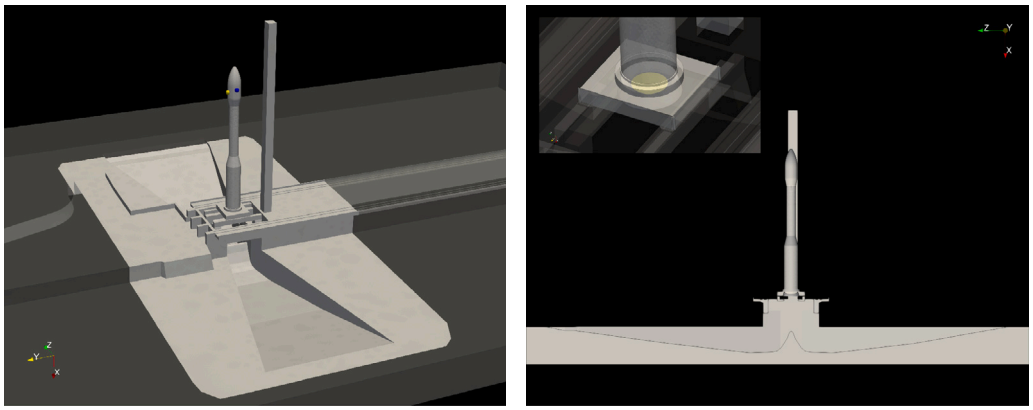

(a) 3D view (b) Plane cut through xz plane and zoom of nozzle patch

Fig. 5. Geometry of the launch pad used for the simulations. On the left, the computational box used is highlighted, and probe 1 and 2 on the fairing are indicated in blue and yellow respectively. On the right, the patch used for nozzle outlet conditions is indicated in yellow in the zoom.

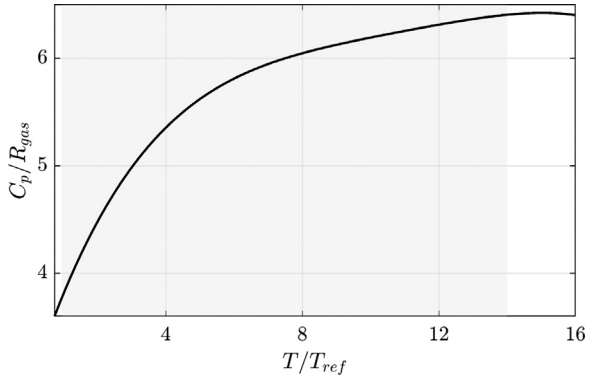

Fig. 6. Normalised specific heat capacity with respect to the non-dimensional temperature with an indication of the range encountered in the field during the simulation.

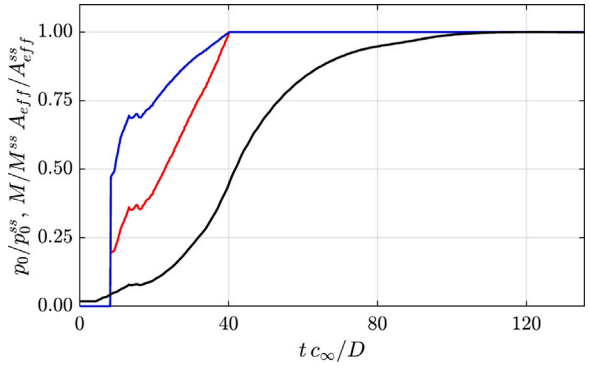

Fig. 7. Ramp of total pressure (—), Mach number (—), and effective area (—) imposed during the simulation at the nozzle exit. The quantities are made non-dimensional with respect to their steady state values.

temperatures and those of the propellant mixture for hot temperatures. The behaviour of the assumed specific heat capacity with respect to the temperature is shown in Fig. 6 with an indication of the range encountered in the field.

The computational domain is a large Cartesian box enclosing the launch pad geometry. Table 2 reports the main characteristics of the simulations. Preliminary computations showed that, although stretched meshes allow an improved resolution of the plume region, they worsen the propagation of sound towards the launcher. Therefore, two uniform grids have been considered, doubling the number of points in each direction, to assess the influence of the resolution on the predicted acoustic field. The boundary conditions are specified as follows:

- generalised characteristic relaxation boundary conditions [50] are applied at the far field to suppress the reflection of pressure waves at the boundaries. This aspect is particularly important to avoid the contamination of the pressure signals on the launcher fairing.
- No-slip, adiabatic boundary conditions are imposed through IBM at the wall.
- The supersonic inflow boundary condition representing the nozzle plume is directly imposed at the nozzle exit section, whose surface (highlighted in the zoom in Fig. 5(b)) is treated as a special patch of the whole immersed solid surface (launcher plus launch pad) according to the method described in Section 2.1. The following procedure is used to establish the conditions assigned to the patch: (i) we establish a realistic ramp of the total pressure, and hence of the nozzle pressure ratio $NPR = p_0/p_\infty$; (ii) on the basis of the instantaneous NPR, we compute the abscissa of the separation point by means of the Schmucker separation criterion [51]; (iii) from the position of the separation point, we evaluate the nozzle area ratio upstream of the separation point and the corresponding Mach number by means of isentropic relations; (iv) we assume the area and the Mach number at that section to be the instantaneous effective area and Mach number of the uniform nozzle jet at the exit section, avoiding simulating the interior volume of the nozzle [52]. The obtained ramp profiles for the quantities involved are reported in Fig. 7.

The simulations reported in this work were performed using 32 nodes (128 GPUs) for mesh A and 128 nodes (512 GPUs) for mesh B. In both cases each GPU processes over 8 million nodes, which guarantees optimal conditions of efficiency.

4. Results

In the following, we report the analysis of the results of the simulations carried out. First we comment the qualitative behaviour of the flow field evolution and then we analyse the overpressure signal on two probes on the launcher's fairing, comparing the results with flight measurements in time and frequency. All the quantities are made non-dimensional assuming as a reference length, velocity and temperature the diameter D of the nozzle exit, the speed of sound of the undisturbed flow and the ambient temperature, respectively.

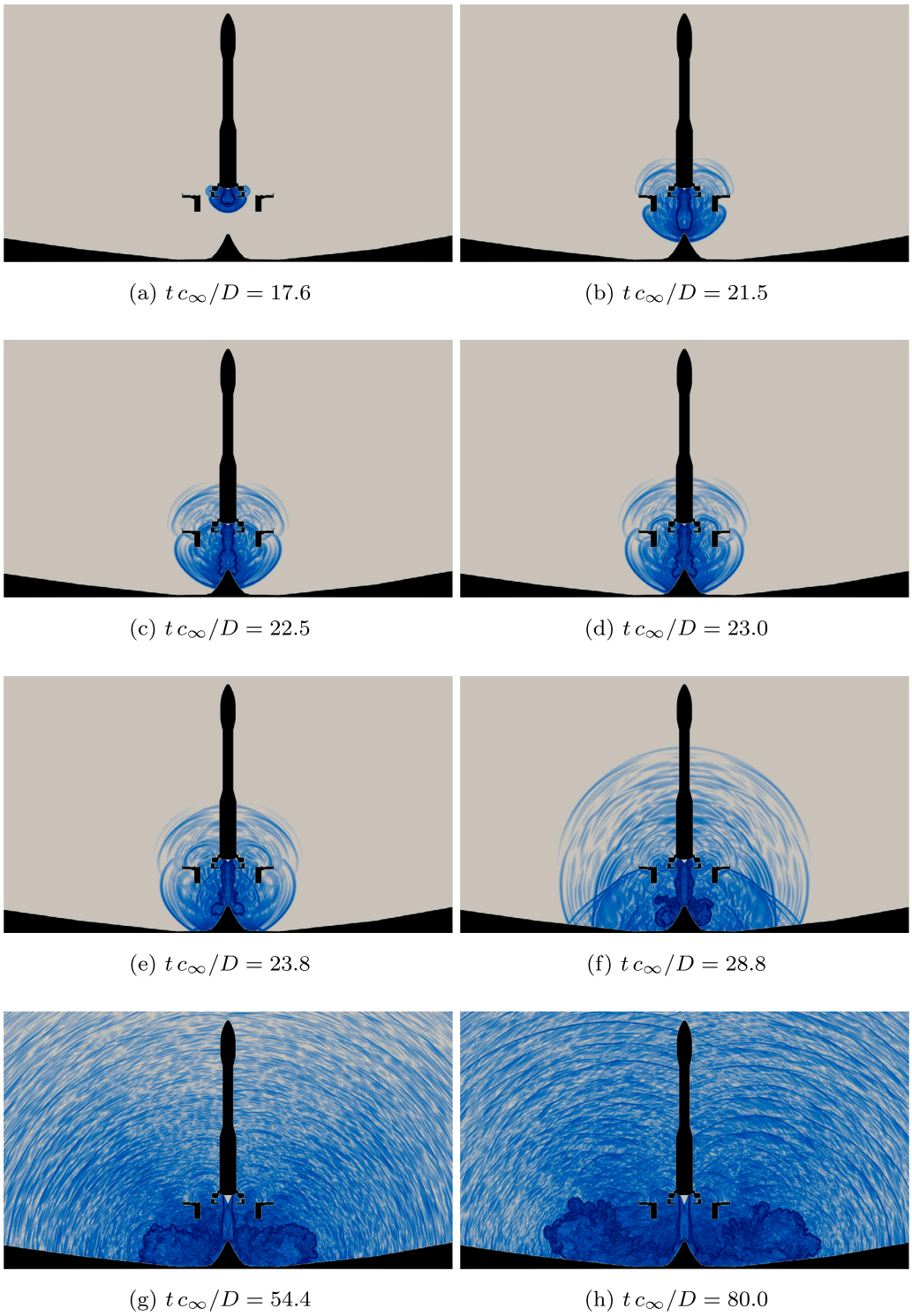

(a) $t\,c_\infty/D = 17.6$ (b) $t\,c_\infty/D = 21.5$

(c) $t\,c_\infty/D = 22.5$ (d) $t\,c_\infty/D = 23.0$

(e) $t\,c_\infty/D = 23.8$ (f) $t\,c_\infty/D = 28.8$

(g) $t\,c_\infty/D = 54.4$ (h) $t\,c_\infty/D = 80.0$

Fig. 8. Snapshots of the density gradient magnitude in logarithmic scale in the xz plane.

4.1. Qualitative behaviour of the flow

Fig. 8 shows the evolution of the flow by means of several snapshots of the density gradient magnitude in logarithmic scale ($\log \|\nabla\rho\|$) in the vertical plane xz (see also video 1 in the additional material).

The compressible starting jet produced by the SRM ignition generates an initial wave that moves downwards towards the flame deflector, interacts with the pad, and evolves (Figs. 8(a)–8(b)). Soon after, the annular shear layer of the jet radiates waves that interact with the interior part of the pad and then advance through the launch pad's openings (Figs. 8(b)–8(d)). In the meantime, the starting jet impacts on the flame deflector and the flow is split laterally along its side walls. From the impact, strong waves are generated (Figs. 8(c)–8(e)) which radiate towards the ambient through both the lateral ducts and the open slots of the pad. Next, the first waves generated by the SRM ignition interact with the duct bottom walls and induce strong reflected waves that propagate with oblique fronts up to and beyond the launch pad (Fig. 8(f)). While the jet reaches its steady state configuration (Fig. 8(g)), with one complete shock cell followed by a bow shock on

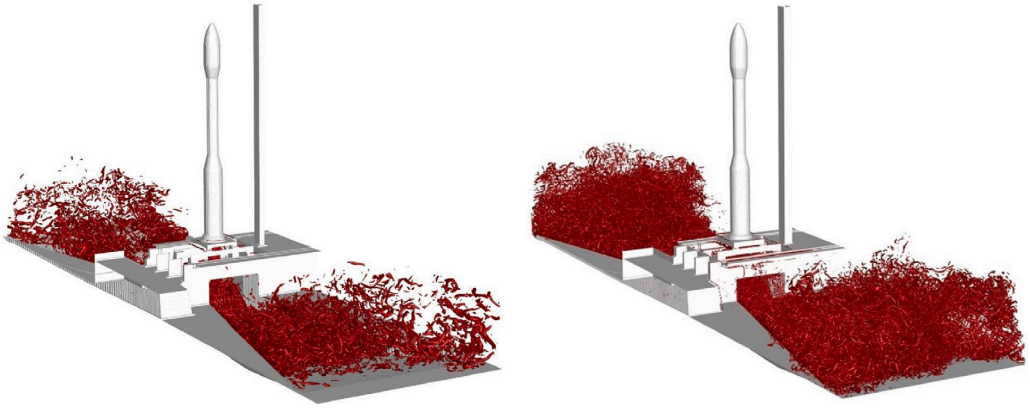

(a) Mesh A (b) Mesh B

Fig. 9. Visualisation of the jet turbulent structures developing along the ducts by means of the Q-criterion.

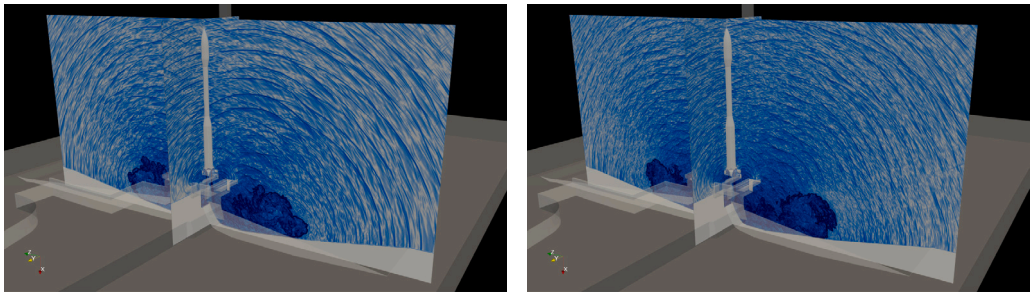

(a) Mesh A (b) Mesh B

Fig. 10. Schlieren-like visualisation on xy and xz planes passing through the center of the nozzle exit section, at time $t\,c_\infty/D = 82.0$.

top of the flame deflector and lateral wall jets (see Brehm et al. [17]), the plume evolves through the ducts with two large vortical structures at the edge of the ejected flow. In addition to the upward travelling waves conveyed steadily through the openings in the launch pad, it is possible to observe for longer times (Fig. 8(h)), how the plume generates acoustic waves that reach the top of the launcher directly (waves from the exiting heads of the plumes) or indirectly (waves refracted by the lateral/external edges of the launch pad walls).

Snapshots in Fig. 9 show a representation of the jet turbulent structures according to the Q-criterion [53] for the two grids, and depicts the transient development of large and fine vortical structures along the evolving plume. From the figure, it is possible to appreciate how the finer grid is better able to represent the richness of the small turbulent structures produced in the field. Fig. 10 reports instead a schlieren-like visualisation for the two grids on the vertical planes xy and xz passing through the center of the nozzle exit section, at time $t\,c_\infty/D = 82.0$. The comparison shows clearly how the increased resolution of mesh B is necessary if one wants to better capture the acoustic waves travelling from the starting jet to the fairing of the launcher. In fact, for the coarse mesh, intense shock waves develop for long times from the plume and finally reach the fairing, inducing relevant pressure fluctuations with a consistent periodicity (see the Fourier analysis in Section 4.2). On the other hand, for the finer grid the same pressure waves are milder and their intensity is comparable with the other waves reaching the top part of the launcher.

4.2. Time evolution and fourier analysis of pressure fluctuations

From a quantitative point of view, in the first place we compare the time evolution of the pressure signals recorded by two probes on the fairing with the corresponding flight data. One probe faces the ducts (indicated in blue in Fig. 5), whereas the other is displayed by 90 degrees (positive y, indicated in yellow in Fig. 5). The comparison in Fig. 11 shows that, especially with the fine grid, the simulations are able to recover with an exceptional degree of accuracy the qualitative and quantitative behaviour of the flight signals despite the challenging scenario. In particular, the trace of the IOP is clearly recognisable in the fluctuations of the first instants $t\,c_\infty/D \approx 45$, while the signature of the DOP is visible from the increased high-frequency fluctuations from $t\,c_\infty/D \approx 80$. As expected, for long times the agreement decreases and numerical results tend to overestimate the low-frequency modulation of the pressure fluctuations. As a matter of fact, the model adopted does not consider aspects like the afterburning of the plume or the presence of alumina particle in the ejected flow, and most of all does not consider the ascent motion of the space launcher. In fact, although the geometry can be considered fixed for the very first instants, which are those of interest to study the IOP/DOP mechanism, when time runs the validity of the assumption fades away and this certainly has a major role in the differences observed.

The sound pressure level (SPL) for the two probes reported in Fig. 12 confirms that also the spectral content of the signals is progressively recovered refining the mesh. In fact, the fine resolution of mesh B allows an extension of the range of the spatial and temporal scales resolved in the simulation, and thus provides a marked improvement in the spectral accuracy at high frequencies. Moreover, as explained in the previous section, when the coarse mesh is considered, the intensity of the pressure waves from the plume is overestimated for long times, which gives rise to a distinct peak in the SPL at $f\,D/c_\infty \approx 0.25$. By improving the resolution, the intensity of these waves is reduced, and so their spectral signature is less important, causing the spurious peak to vanish. Increasing even more the resolution would have certainly pushed further the cut-off induced by the ILES methodology

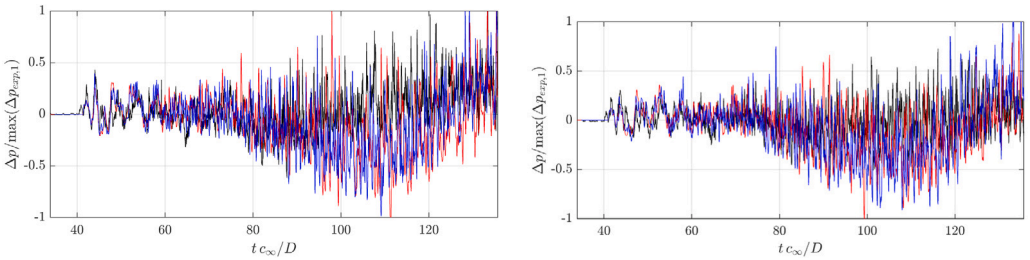

(a) Probe 1. (b) Probe 2.

Fig. 11. Non-dimensional pressure fluctuations at probe 1 and probe 2. Flight data —, Mesh A —, Mesh B —.

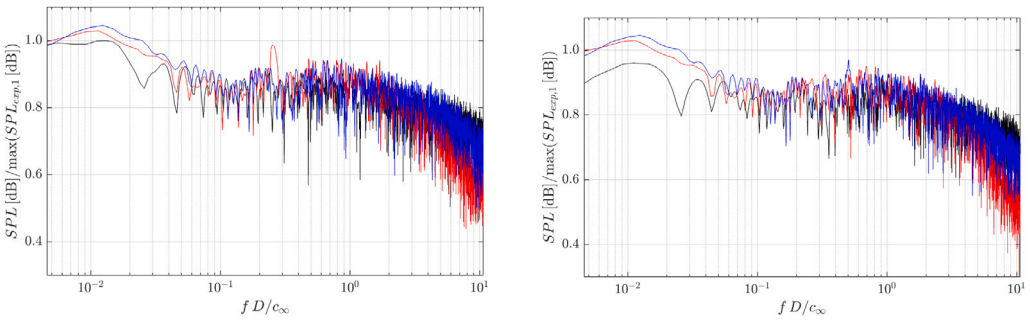

(a) Probe 1. (b) Probe 2.

Fig. 12. Sound Pressure Level at probe 1 and probe 2, normalised by the maximum of the SPL at probe 1 of the flight data. Flight data —, Mesh A —, Mesh B —.

adopted. However, this would have also caused a significant increase in computational cost, and since the results obtained with the fine mesh already show a remarkable agreement with the flight data, we have not considered another, finer grid. On the other end, given the explained lack of accuracy for long times, the spectra at low frequencies is not reliable and rather overestimated, especially for the probe not facing the ducts which perceives a reduced level of fluctuations.

4.3. Wavelet analysis of pressure fluctuations

Fourier analysis is certainly useful to examine the overall frequency content of signals, and also in our case it provided us with relevant general information about the pressure fluctuations. However, given the transient nature of the phenomenon under study, such an analysis is not able to distinguish mechanisms that are highly localised in time, like the IOP/DOP mechanisms. In fact, if highly unsteady and irregular time series are considered, Fourier transform may disguise features of the signal in a time-averaged sense and thus misrepresent the actual physical phenomena behind the signal [54]. Other tools exist to study multi-scale and non-stationary processes, and among them wavelet analysis [55,56] is a widely considered option. For this reason, in order to individuate and characterise the IOP/DOP mechanisms, we here study the pressure signals recorded by the probes by means of wavelet analysis. The interested reader can find a complete presentation of the wavelet theory in several works [57,58], whereas their specific use in fluid mechanics is reported in Farge [27] and Lewalle [59]. In the following, we report only the essential elements needed to understand the results presented in this work.

The wavelet transform of a continuous signal $w(t)$ is defined as:

$$W_\Psi(k,\tau) = \frac{1}{\sqrt{k}} \int_{-\infty}^{+\infty} w(t) \Psi^* \left(\frac{t-\tau}{k} \right) dt\,, \tag{6}$$

where Ψ is the wavelet mother function, k is a dilatation parameter, τ is the time-translation parameter and $*$ indicates the complex conjugate. By comparing the original signal with the scaled (with wavelet scale k) and translated (with time shift τ) version of the wavelet mother function, it is possible to describe not only the amplitude of a certain feature at a certain scale, but also how that specific contribution evolves in time. For a discrete signal w_n with $n = 1, \dots, N$ samples, it is possible to define the continuous wavelet transform as [60]:

$$W_n(k) = \sum_{n'=0}^{N-1} w_{n'} \Psi^* \left[\frac{(n'-n)dt}{k} \right]. \tag{7}$$

As usually done in turbulence, we use the Morlet wavelet mother function, because of its higher resolution in frequency with respect to other mother functions. The complex Morlet wavelet function is equal to:

$$\Psi(t) = \pi^{-1/4} e^{i\omega_0 t} e^{-t^2/2} \tag{8}$$

with ω_0 being the non-dimensional frequency, equal to 6 to satisfy the admissibility condition [27]. It is possible to demonstrate that the wavelet transform at a given scale k can be seen as a band-pass filter in the Fourier space. Moreover, an equivalent Fourier period – and hence frequency – can be related analytically with the wavelet scale, through the method proposed by Meyers et al. [61]. As a result, wavelet analysis makes it possible to define a localised counterpart in the time/frequency domain of the standard Fourier spectra, tracking the time evolution of the frequency content of the signal. The algorithms adopted to compute the wavelet transform in this work are documented in Torrence and Compo [60].

The comparison of the obtained wavelet coefficients squared allows the identification of the most energetic events in the time–frequency domain, or more properly the time-time scale domain, in the so called scalograms. The comparisons of the scalograms of the measured and numerical pressure signals, reported in the top row of Fig. 13 (probe 1) and 14 (probe 2), show that, despite the fine resolution and the relevant computational resources used, there are still some discrepancies between the simulated results and the measured ones. Nonetheless, the simulations are fully able to capture the most significant energetic events associated with IOP and DOP and to characterise their time and

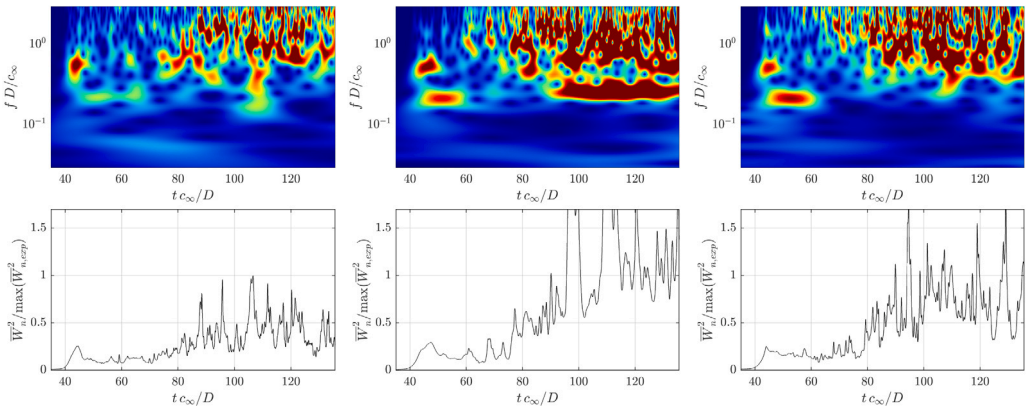

(a) Flight data. (b) Mesh A. (c) Mesh B.

Fig. 13. Wavelet scalograms (top row) and scale-averaged scalograms (bottom row) for probe 1. Scale-averaged scalograms are normalised by the maximum for probe 1.

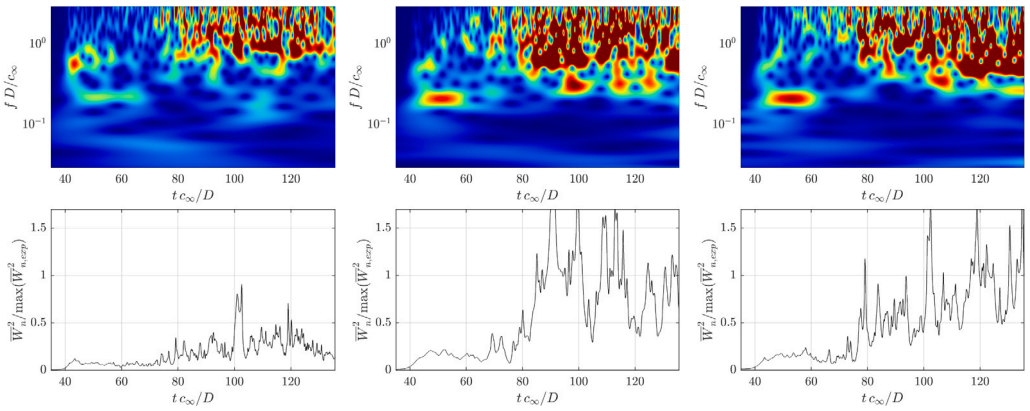

(a) Flight data. (b) Mesh A. (c) Mesh B.

Fig. 14. Wavelet scalograms (top row) and scale-averaged scalograms (bottom row) for probe 2. Scale-averaged scalograms are normalised by the maximum for probe 1.

time scales. In particular, the highly energetic event at low frequency approximately at $t\,c_\infty/D \approx 45$ is related to the pressure waves induced by the ignition overpressure, which are significant if the launch pad is open, whereas the intermittent events in the following instants are related to more turbulent phenomena and to the acoustic waves generated in correspondence of the duct openings, namely the DOP (see Fig. 8).

The scale-averaged scalograms in the bottom row of Figs. 13 and 14 makes even more evident the increase in quality of the results for the fine grid and the ability of both simulations to describe the ignition and duct overpressure phenomena in qualitative and quantitative terms, especially for times smaller than $t\,c_\infty/D \approx 80$. Nonetheless, even for larger times, the wavelet analysis shows that simulations are still able to capture the presence of relevant phenomena, like those at $t\,c_\infty/D \approx 100$ and $t\,c_\infty/D \approx 120$.

5. Conclusions

The significant acceleration provided by GPUs has boosted the performance of our solver STREAmS and has made it possible, by means of IBM, to replicate the aeroacoustics at lift-off of a realistic space launchers on a realistic launch pad by means of a single, unsteady, high-fidelity Large Eddy Simulation, with a direct computation of sound.

The results, especially for the finer grid, demonstrates satisfactory agreement with the flight data, despite the challenging conditions. Levels of pressure fluctuations in the first instants of the ignition are correctly predicted both in time and in frequency, although some differences exist for long times, since the launcher actually moves from the still position that is assumed in the simulation. Through wavelet analysis, we then showed how we can identify and pinpoint the IOP and DOP mechanisms, and we confirmed that the numerical results can predict with satisfactory accuracy the time and frequency content of the most energetic events in the pressure fluctuations on the fairing of the space launcher.

The availability of the flow variables throughout the ignition and for the entire domain, makes it possible to envisage in future works a more in-depth analysis for the identification of the noise sources, using for example causality methods [17] or decomposing the pressure field in its hydrodynamic and acoustic components using methods like the one presented in Mancinelli et al. [62]. Moreover, the availability of such a numerical framework makes it possible to predict and assess the effects of possible solutions to mitigate the effects of IOP/DOP mechanisms.

Declaration of competing interest

The authors declare the following financial interests/personal relationships which may be considered as potential competing interests: Giacomo Della Posta, Fulvio Stella, Matteo Bernardini reports financial support was provided by European Space Agency.

Data availability

The authors do not have permission to share data.

Acknowledgement

The present study has been carried out in the framework of the program Work Order 3, ESA Contract No. 4000120618/17/I/AL. We acknowledge the CINECA computing centre for having provided us with the computational resources required by this work.

Appendix A. Supplementary data

Supplementary material related to this article can be found online at https://doi.org/10.1016/j.compfluid.2023.105945.

References

[1] Mortain F, Cléro F, Palmieri D. Full scale acoustic source identification on VEGA launch pad at lift-off. In: ICSV26. MONTREAL, Canada; 2019, URL https://hal.archives-ouvertes.fr/hal-02333532.
[2] Ikawa H, Laspesa FS. Ignition/duct overpressure induced by space shuttle solid rocket motor ignition. J Spacecr Rockets 1985;22(4):481–8. http://dx.doi.org/10.2514/3.25776.
[3] Jiang C, Han T, Gao Z, Lee C-H. A review of impinging jets during rocket launching. Prog Aerosp Sci 2019;109:100547. http://dx.doi.org/10.1016/j.paerosci.2019.05.007.
[4] Panda J, Mosher RN, Porter BJ. Noise source identification during rocket engine test firings and a rocket launch. J Spacecr Rockets 2014;51(6):1761–72. http://dx.doi.org/10.2514/1.A32863.
[5] Gély D, Elias G, Mascanzoni F, Foulon H. Acoustic environment of the VEGA launch vehicle at lift-off. In: Proceedings of the forum acusticum, budapest. 2005.
[6] Panda J, Mosher R. Microphone phased array to identify liftoff noise sources in model-scale tests. J Spacecr Rockets 2013;50(5):1002–12. http://dx.doi.org/10.2514/1.A32433.
[7] Karthikeyan N, Venkatakrishnan L. Acoustic characterization of jet interaction with launch structures during lift-off. J Spacecr Rockets 2017;54(2):356–67. http://dx.doi.org/10.2514/1.A33616.
[8] Kwak D, Kiris C. Current CFD practices in launch vehicle applications. Tech. Rep. 20120013092, NASA; 2012.
[9] Colonius T, Lele SK. Computational aeroacoustics: progress on nonlinear problems of sound generation. Prog Aerosp Sci 2004;40(6):345–416. http://dx.doi.org/10.1016/j.paerosci.2004.09.001.
[10] Tam CKW. Supersonic jet noise. Annu Rev Fluid Mech 1995;27(1):17–43. http://dx.doi.org/10.1146/annurev.fl.27.010195.000313.
[11] Gröschel E, Schröder W, Renze P, Meinke M, Comte P. Noise prediction for a turbulent jet using different hybrid methods. Comput & Fluids 2008;37(4):414–26. http://dx.doi.org/10.1016/j.compfluid.2007.02.010, Turbulent Flow and Noise Generation.
[12] Labbé O, Peyret C, Rahier G, Huet M. A CFD/CAA coupling method applied to jet noise prediction. Comput & Fluids 2013;86:1–13. http://dx.doi.org/10.1016/j.compfluid.2013.07.013.
[13] Jaunet V, Mancinelli M, Jordan P, Towne A, Edgington-Mitchell DM, Lehnasch G, et al. Dynamics of round jet impingement. In: 25th AIAA/CEAS aeroacoustics conference. 2019, p. 2769. http://dx.doi.org/10.2514/6.2019-2769.
[14] Varé M, Bogey C. Flow and acoustic fields of rocket jets impinging on a perforated plate. AIAA J 2022;1–14. http://dx.doi.org/10.2514/1.J061253.
[15] Nonomura T, Goto Y, Fujii K. Aeroacoustic waves generated from a supersonic jet impinging on an inclined flat plate. Int J Aeroacoust 2011;10(4):401–25. http://dx.doi.org/10.1260/1475-472X.10.4.401.
[16] Nonomura T, Honda H, Nagata Y, Yamamoto M, Morizawa S, Obayashi S, et al. Plate-angle effects on acoustic waves from supersonic jets impinging on inclined plates. AIAA J 2016;54(3):816–27. http://dx.doi.org/10.2514/1.J054152.
[17] Brehm C, Housman JA, Kiris CC. Noise generation mechanisms for a supersonic jet impinging on an inclined plate. J Fluid Mech 2016;797:802–50. http://dx.doi.org/10.1017/jfm.2016.244.
[18] Tsutsumi S, Takaki R, Shima E, Fujii K, Arita M. Generation and propagation of pressure waves from H-IIA launch vehicle at lift-off. In: 46th AIAA aerospace sciences meeting and exhibit. 2012, http://dx.doi.org/10.2514/6.2008-390.
[19] Kiris CC, Housman JA, Barad MF, Brehm C, Sozer E, Moini-Yekta S. Computational framework for launch, ascent, and vehicle aerodynamics (LAVA). Aerosp Sci Technol 2016;55:189–219. http://dx.doi.org/10.1016/j.ast.2016.05.008.
[20] Slotnick JP, Khodadoust A, Alonso J, Darmofal D, Gropp W, Lurie E, et al. CFD vision 2030 study: A path to revolutionary computational aerosciences. Tech. Rep. 20140003093, NASA; 2014.
[21] Pavish D, Deese J. CFD analysis of unsteady ignition overpressure effects on Delta II and III launch vehicles. In: 18th Applied aerodynamics conference. 2000, http://dx.doi.org/10.2514/6.2000-3922.
[22] Majamaki A, Lee J. CFD simulations of launch environments for delta IV vehicles at the SLC-6 launch pad. In: 49th AIAA aerospace sciences meeting including the new horizons forum and aerospace exposition. 2012, http://dx.doi.org/10.2514/6.2011-1236.
[23] Escartí-Guillem MS, García-Raffi LM, Hoyas S. URANS analysis of a launch vehicle aero-acoustic environment. Appl Sci 2022;12(7). http://dx.doi.org/10.3390/app12073356.
[24] Troclet B, Alestra S, Terrasse I, Jeanjean S, Srithammavanh V. Identification of overpressure sources at launch vehicle liftoff using an inverse method. J Spacecr Rockets 2007;44(3):597–606. http://dx.doi.org/10.2514/1.21577.
[25] Bianchi S. VEGA, the European small launcher: Development status, future perspectives, and applications. Acta Astronaut 2008;63(1):416–27. http://dx.doi.org/10.1016/j.actaastro.2007.12.058.
[26] European Space Agency. Vega qualification flight VV01. 2012, URL https://download.esa.int/docs/VEGA/Vega_PressKit_06-02-2012_EN.pdf.
[27] Farge M. Wavelet transforms and their applications to turbulence. Annu Rev Fluid Mech 1992;24(1):395–458. http://dx.doi.org/10.1146/annurev.fl.24.010192.002143.
[28] Grizzi S, Camussi R. Wavelet analysis of near-field pressure fluctuations generated by a subsonic jet. J Fluid Mech 2012;698:93–124. http://dx.doi.org/10.1017/jfm.2012.64.
[29] Jaunet V, Collin E, Bonnet J-P. Wavelet series method for reconstruction and spectral estimation of laser Doppler velocimetry data. Exp Fluids 2012;52(1):225–33. http://dx.doi.org/10.1007/s00348-011-1222-z.
[30] Camussi R, Di Marco A, Castelain T. Statistical analysis of the hydrodynamic pressure in the near field of compressible jets. Int J Heat Fluid Flow 2017;64:1–9. http://dx.doi.org/10.1016/j.ijheatfluidflow.2017.01.007.
[31] Martelli E, Ciottoli P, Bernardini M, Nasuti F, Valorani M. Detached eddy simulation of shock unsteadiness in an over-expanded planar nozzle. AIAA J 2017;55(6):2016–28. http://dx.doi.org/10.2514/1.J055273.
[32] Bernardini M, Della Posta G, Salvadore F, Martelli E. Unsteadiness characterisation of shock wave/turbulent boundary-layer interaction at moderate Reynolds number. J Fluid Mech 2023;954:A43. http://dx.doi.org/10.1017/jfm.2022.1038.
[33] Vega VV01 on launch pad, Copyright: S. Corvaja, ESA. 2023, https://www.esa.int/var/esa/storage/images/esa_multimedia/images/2012/01/vega_vv01_on_launch_pad/9944464-2-eng-GB/Vega_VV01_on_launch_pad_pillars.jpg, Accessed: 28-04-2023.
[34] Bernardini M, Modesti D, Salvadore F, Pirozzoli S. STREAmS: A high-fidelity accelerated solver for direct numerical simulation of compressible turbulent flows. Comput Phys Comm 2021;263:107906. http://dx.doi.org/10.1016/j.cpc.2021.107906.
[35] Bernardini M, Modesti D, Salvadore F, Sathyanarayana S, Della Posta G, Pirozzoli S. STREAmS-2.0: Supersonic turbulent accelerated Navier-Stokes solver version 2.0. Comput Phys Comm 2023;285:108644. http://dx.doi.org/10.1016/j.cpc.2022.108644.
[36] Sathyanarayana S, Bernardini M, Modesti D, Pirozzoli S, Salvadore F. High-speed turbulent flows towards the exascale: STREAmS-2 porting and performance. 2023, arXiv:2304.05494.
[37] Grinstein FF, Margolin LG, Rider WJ. Implicit large eddy simulation, Vol. 10. CUP; 2007.
[38] Shur ML, Spalart PR, Strelets MK. Noise prediction for increasingly complex jets. Part I: Methods and tests. Int J Aeroacoust 2005;4(3):213–45. http://dx.doi.org/10.1260/1475472054771376.
[39] Shur ML, Spalart PR, Strelets MK. Noise prediction for increasingly complex jets. Part II: Applications. Int J Aeroacoust 2005;4(3):247–66. http://dx.doi.org/10.1260/1475472054771385.
[40] Pirozzoli S. Generalized conservative approximations of split convective derivative operators. J Comput Phys 2010;229(19):7180–90. http://dx.doi.org/10.1016/j.jcp.2010.06.006.
[41] Jiang G-S, Shu C-W. Efficient implementation of weighted ENO schemes. J Comput Phys 1996;126(1):202–28. http://dx.doi.org/10.1006/jcph.1996.0130.
[42] Borges R, Carmona M, Costa B, Don WS. An improved weighted essentially non-oscillatory scheme for hyperbolic conservation laws. J Comput Phys 2008;227(6):3191–211. http://dx.doi.org/10.1016/j.jcp.2007.11.038.
[43] Nam J, Lien F. A ghost-cell immersed boundary method for large-eddy simulations of compressible turbulent flows. Int J Comput Fluid Dyn 2014;28(1–2):41–55. http://dx.doi.org/10.1080/10618562.2014.887072.
[44] Piquet A, Roussel O, Hadjadj A. A comparative study of brinkman penalization and direct-forcing immersed boundary methods for compressible viscous flows. Comput & Fluids 2016;136:272–84. http://dx.doi.org/10.1016/j.compfluid.2016.06.001.
[45] Bernardini M, Modesti D, Pirozzoli S. On the suitability of the immersed boundary method for the simulation of high-Reynolds-number separated turbulent flows. Comput & Fluids 2016;130:84–93. http://dx.doi.org/10.1016/j.compfluid.2016.02.018.
[46] Bernardini M, Cimini M, Stella F, Cavallini E, Di Mascio A, Neri A, et al. Implicit large-eddy simulation of solid rocket motors using the immersed boundary method. In: AIAA propulsion and energy 2021 forum. 2021, http://dx.doi.org/10.2514/6.2021-3696.
[47] Project TC. CGAL user and reference manual. 5.5.2. CGAL Editorial Board; 2023, URL https://doc.cgal.org/5.5.2/Manual/packages.html.
[48] De Vanna F, Picano F, Benini E. A sharp-interface immersed boundary method for moving objects in compressible viscous flows. Comput & Fluids 2020;201:104415. http://dx.doi.org/10.1016/j.compfluid.2019.104415.

[49] Chaudhuri A, Hadjadj A, Chinnayya A. On the use of immersed boundary methods for shock/obstacle interactions. J Comput Phys 2011;230(5):1731–48. http://dx.doi.org/10.1016/j.jcp.2010.11.016.
[50] Pirozzoli S, Colonius T. Generalized characteristic relaxation boundary conditions for unsteady compressible flow simulations. J Comput Phys 2013;248:109–26. http://dx.doi.org/10.1016/j.jcp.2013.04.021.
[51] Schmucker R. Strömungsvorgänge beim betrieb überexpandierter düsen chemischer raketentriebwerke, teil 1: Strömungsablösung. 1973, Bericht TB-10, Technische UniversitÄT MÜNchen.
[52] Gusman M, Housman J, Kiris C. Best practices for CFD simulations of launch vehicle ascent with plumes - OVERFLOW perspective. In: 49th AIAA aerospace sciences meeting including the new horizons forum and aerospace exposition. 2011, p. 1054. http://dx.doi.org/10.2514/6.2011-1054.
[53] Dubief Y, Delcayre F. On coherent-vortex identification in turbulence. J Turbul 2000;1:N11. http://dx.doi.org/10.1088/1468-5248/1/1/011.
[54] Huang NE, Shen Z, Long SR, Wu MC, Shih HH, Zheng Q, et al. The empirical mode decomposition and the Hilbert spectrum for nonlinear and non-stationary time series analysis. Proc R Soc London Ser A, Math Phys Sci 1998;454(1971):903–95. http://dx.doi.org/10.1098/rspa.1998.0193.
[55] Mallat S. A theory for multiresolution signal decomposition: the wavelet representation. IEEE Trans Pattern Anal Mach Intell 1989;11(7):674–93. http://dx.doi.org/10.1109/34.192463.
[56] Daubechies I. Ten lectures on wavelets. SIAM; 1992, http://dx.doi.org/10.1137/1.9781611970104.
[57] Kaiser G, Hudgins LH. A friendly guide to wavelets, Vol. 300. Springer; 1994.
[58] Mallat S. A wavelet tour of signal processing. Elsevier; 1999.
[59] Lewalle J. Wavelet transforms of some equations of fluid mechanics. Acta Mech 1994;104(1):1–25. http://dx.doi.org/10.1007/BF01170275.
[60] Torrence C, Compo GP. A practical guide to wavelet analysis. Bull Am Meteorol 1998;79(1):61–78. http://dx.doi.org/10.1175/1520-0477(1998)079<0061:APGTWA>2.0.CO;2.
[61] Meyers SD, Kelly BG, O'Brien JJ. An introduction to wavelet analysis in oceanography and meteorology: With application to the dispersion of yanai waves. Mon Weather Rev 1993;121(10):2858–66. http://dx.doi.org/10.1175/1520-0493(1993)121<2858:AITWAI>2.0.CO;2.
[62] Mancinelli M, Pagliaroli T, Di Marco A, Camussi R, Castelain T. Wavelet decomposition of hydrodynamic and acoustic pressures in the near field of the jet. J Fluid Mech 2017;813:716–49. http://dx.doi.org/10.1017/jfm.2016.869.